Full-wave vector Maxwell equation modeling of the self-focusing of ultrashort optical pulses in a nonlinear Kerr medium exhibiting a finite response time

Richard W. Ziolkowski and Justin B. Judkins

Department of Electrical and Computer Engineering, University of Arizona, Tuscon, Arizona 85721

Received March 26, 1992; revised manuscript received July 1, 1992

The extension of the conventional finite-difference time-domain solution of the full vector Maxwell equations to modeling femtosecond optical-pulse propagation in a nonlinear Kerr medium that exhibits a finite response time is presented. Numerical results are given for nonlinear self-focusing in two space dimensions and time; the technique can be generalized to three space dimensions with adequate computer resources. Comparisons with previously reported and anticipated results are made. Several novel phenomena that are not observed with scalar models of self-focusing and that can be attributed only to the complete solution of the vector Maxwell equations are discussed.

INTRODUCTION

The nonlinear self-focusing of optical beams has been known for more than two decades,[1-6] but the only time-dependent theories that were advanced to describe the phenomena were based on a variety of lower-dimensional and scalar models, including the paraxial wave equation[2,7,8] or modifications of it.[9,10] With continuing and heightened interest in nonlinear semiconductor and optically integrated devices, more-accurate and realistic numerical simulations of these devices and systems are in demand. Until recently practical full-wave analyses of the vector, space–time Maxwell equations were not available even in the linear regime. Algorithm and hardware developments now provide a means to achieve fully three-dimensional vector approaches to extremely complex linear time-domain electromagnetics problems and the potential for applications of these techniques to the more difficult and demanding nonlinear problems.

In this paper we report the modeling in two space dimensions and time of self-focusing of an ultrashort pulsed beam in a nonlinear Kerr material with a finite response time; the model uses a generalization of a standard, finite-difference time-domain (FDTD), full-wave, vector, linear Maxwell's equation solver. A currently used phenomenological time relaxation (Debye) model of a nonlinear Kerr material was incorporated with the electromagnetic FDTD solver so that the effects of finite response times could be studied. It will be shown that the full-wave, vector approach recovers the physical effects that are predicted with standard scalar-equation models of the self-focusing phenomena. In addition, we report a number of effects that are not recoverable from those scalar models. Comparisons with anticipated simulation and known experimental results are made.

There have been a number of recently reported numerical solutions of the full-wave, vector, time-independent Maxwell equations[11-14] and of vector paraxial equations.[15-17] These efforts have provided, for instance, the modal fields and the propagation of beams in nonlinear waveguides. In contrast, the following time-dependent analysis accounts for the complete time evolution of the system as a pulse propagates in a Kerr medium with a finite response time; in particular, the analysis provides a complete picture of the pulse behavior during the nonlinear self-focusing process. Note that because of the nonlinearities such a pulse solution cannot be obtained from any sequence of single-frequency, time-independent results; it can only be obtained from a direct time integration of Maxwell's equations. Thus the time-independent and the time-dependent approaches yield additional and complementary information.

In addition, we note that the nonlinear FDTD approach presented below accounts for all the nonlinear effects induced by the presence of the Kerr medium. However, we have not yet included linear dispersion in our model, nor do we claim to be modeling all possible nonlinear materials. There are, of course, materials for which the dispersive rather than the nonlinear effects dominate. Nonetheless, the following results are applicable to materials in which the nonlinear effects dominate the dispersive effects; the results apply, for instance, to dispersive media in which the propagation distance is shorter than the dispersion length. Since we are trying to discover what new phenomena may occur when the full vector nature of Maxwell's equations is taken into account, we choose to include the nonlinear-medium effects first. As is noted, linear dispersion effects can be straightforwardly incorporated into the nonlinear FDTD approach. The versatility of the FDTD approach is one of its strong characteristics. More-complex media can be readily modeled simply by incorporating a model of more-complex materials.

FULL-WAVE VECTOR MAXWELL'S EQUATIONS

Transverse Magnetic Case

By leaving Maxwell's equations in first-order form, we do not ignore the vector properties of the solution and the sources and couplings induced by the nonlinear polariza-

0740-3224/93/020186-13$05.00

tion terms. In particular, a TM-polarized wave has the components (E_x, E_z, H_y). In two space dimensions and time with coordinates (x, z, t) and with the choice of these TM field components, Maxwell's equations reduce to the form

$$\partial_t H_y = -\frac{1}{\mu_0}(\partial_z E_x - \partial_x E_z), \tag{1}$$

$$\partial_t E_x = -\frac{1}{\epsilon_{\text{eff}}}\partial_z H_y - \frac{\sigma_{\text{eff}}}{\epsilon_{\text{eff}}}E_x, \tag{2}$$

$$\partial_t E_z = +\frac{1}{\epsilon_{\text{eff}}}\partial_x H_y - \frac{\sigma_{\text{eff}}}{\epsilon_{\text{eff}}}E_z, \tag{3}$$

where the effective permittivity and the conductivity of the Kerr medium are

$$\epsilon_{\text{eff}} = \epsilon_{\text{L}} + \epsilon_0 \chi^{\text{NL}} \tag{4}$$

$$\sigma_{\text{eff}} = \epsilon_0 \partial_t \chi^{\text{NL}}, \tag{5}$$

with χ^{NL} being the third-order nonlinear susceptibility of the medium. Below, since the effective conductivity σ_{eff} depends only on the nonlinear susceptibility, we refer to σ_{eff} as the nonlinear conductivity. The divergence equation associated with this system exhibits a nonlinear source term:

$$\nabla \cdot \mathbf{D}^{\text{L}} = -\nabla \cdot \mathbf{P}^{\text{NL}}, \tag{6}$$

where

$$\mathbf{D}^{\text{L}} = \epsilon_{\text{L}} \mathbf{E}, \tag{7}$$

$$\mathbf{P}^{\text{NL}} = \chi^{\text{NL}}(\mathbf{r}, t, |\mathbf{E}|^2)\mathbf{E}. \tag{8}$$

The definition of χ^{NL} is dependent on the medium model and is discussed below.

Transverse Electric Case

In contrast to the TM case, a TE-polarized wave has the components (E_y, H_x, H_z). In two dimensions and time with coordinates (x, z, t) Maxwell's equations reduce to their TE form:

$$\partial_t H_x = +\frac{1}{\mu_0}\partial_z E_y, \tag{9}$$

$$\partial_t H_z = -\frac{1}{\mu_0}\partial_x E_y, \tag{10}$$

$$\partial_t E_y = +\frac{1}{\epsilon_{\text{eff}}}(\partial_z H_x - \partial_x H_z) - \frac{\sigma_{\text{eff}}}{\epsilon_{\text{eff}}}E_y, \tag{11}$$

where the effective permittivity and conductivity of the Kerr medium are again given by Eqs. (4) and (5). The divergence equation associated with this system also exhibits a nonlinear source term as given by Eqs. (6)–(8).

Medium Model

If the time scale over which the medium changes is greater than the pulse width, one must take into account the effects of the finite response time of the medium. One can treat the nonlinear effect with a finite response time as well as in an instantaneous manner by solving the phenomenological susceptibility equation simultaneously with Maxwell's equations:

$$\partial_t \chi^{\text{NL}} + \frac{1}{\tau}\chi^{\text{NL}} = \frac{1}{\tau}\epsilon_2 |\mathbf{E}|^2, \tag{12}$$

which means, explicitly,

TM case,

$$\partial_t \chi^{\text{NL}} + \frac{1}{\tau}\chi^{\text{NL}} = \frac{1}{\tau}\epsilon_2(|E_x|^2 + |E_z|^2), \tag{13}$$

TE case,

$$\partial_t \chi^{\text{NL}} + \frac{1}{\tau}\chi^{\text{NL}} = \frac{1}{\tau}\epsilon_2 |E_y|^2. \tag{14}$$

The relaxation time τ is variable and represents the response time of the medium. For instance, if T represents the pulse width, then by setting $T \geq \tau$ one obtains an instantaneous-response model: $\chi^{\text{NL}} \approx \epsilon_2 |\mathbf{E}|^2$, i.e., the medium follows the pulse. On the other hand, if $T \ll \tau$, then the finite-response-time effects are maximal and the medium's response significantly lags behind the pulse. Since the electronic properties of materials have relaxation times of the order of 1–10 fs, the instantaneous regime is the most appropriate for most optical systems. However, there are a number of pulsed laser systems available now in this regime, and the trend is toward the development of subfemtosecond systems. For these systems the finite-response-time effects under discussion here will play a significant role. As we demonstrate below, the present analysis can treat both extremes.

Note that we take $\epsilon_L = \epsilon_0$ below. This means that we ignore linear dispersion for the present analysis. Since we are investigating what new phenomena may occur when the full vector nature of Maxwell's equations is taken into account, the nonlinear-medium effects were included first. Linear dispersion was incorporated into the FDTD approach with a number of techniques in the linear regime.[18–20] The approach was recently extended to the nonlinear regime.[21] Because of the versatility of the FDTD approach, we are able to turn on the dispersion effects to analyze their effect on the self-focusing process. These dispersive effects will be incorporated into the next phase of our nonlinear investigations.

Preliminary Analysis

The TM and TE system of equations have some immediate advantages. In particular, they readily accommodate the nonlinear channeling phenomena associated with self-focusing. The development of a nonlinear channel produces a waveguiding condition that will favor propagation of the higher frequencies through the channel. As a result, longer-wavelength components should be removed from the pulse through scattering to large angles and reflections from the throat of the waveguide channel. In addition, the pulse will exchange energy with the medium as the channel forms, owing to the nonlinear conductivity term. The pulse components whose wave numbers have been converted to extremely large values become nonpropagating (evanescent) and dissipate energy to the medium. The nonlinearity also causes frequency conversions that lead to a compression of the pulse. If there is no linear dispersion present in the medium, the compression will not occur on the leading edge of the pulse, and only an upshift (anti-Stokes) in frequencies will be realized. Thus the focal region can be viewed as a high contrast,

lossy dielectric region in which a steepening of the pulse occurs.

From the equation system one can also anticipate a self-limiting effect when the intensity level becomes extremely high. In that high-intensity limit the full-wave vector Maxwell equations allow the longitudinal electric-field component to grow to a substantial level. This growth will create a power flow transverse to the propagation direction as the focal regions are approached. The result is less intensity's being available for, hence the limiting of, the self-focusing process. This physical effect is absent in all scalar models. For instance, Feit and Fleck's[10] nonparaxial algorithm does not account for the longitudinal field components and simply removes from the problem the nonpropagating large-wave-number components that arise when self-focusing is developing. The full-wave approach has no such nonphysical loss mechanism. The mechanism for the transfer of energy from the transverse field components to the longitudinal ones is present in the TM case presented here; the TE case, by definition, has no longitudinal electric-field components.

Additionally, when the linear–nonlinear interface problem is treated, Maxwell's equations will naturally provide the boundary conditions appropriate for this lossy dielectric interface. The tangential field components must be continuous across the interface for all times, e.g., $\hat{n} \times (\mathbf{E}_{\mathrm{NL}} - \mathbf{E}_{\mathrm{L}}) = 0$, where $\hat{n}$ is the unit normal to the interface point from the linear to the nonlinear region; and the normal component must satisfy for all times the condition

$$\hat{n} \cdot (\epsilon_{\mathrm{eff}} \partial_t \mathbf{E}_{\mathrm{NL}} + \sigma_{\mathrm{eff}} \mathbf{E}_{\mathrm{NL}}) = \hat{n} \cdot (\epsilon_{\mathrm{eff}} \partial_t \mathbf{E}_L + \sigma_{\mathrm{eff}} \mathbf{E}_L). \quad (15)$$

Thus the linear–nonlinear interface problem can be handled without any additional constraints' being imposed on the fields.

Analytical representations of the solutions, for instance, of Eqs. (1)–(8) and (13) are readily obtained that permit a qualitative description of the self-focusing effects. For instance, the nonlinear susceptibility and the electric-field components in the TM case satisfy

$$\chi^{\mathrm{NL}} = \exp[-(t/\tau)] \int_0^t dt' \exp[+(t'/\tau)] \frac{\epsilon_2}{\tau} |\mathbf{E}|^2, \quad (16)$$

$$E_x = -\exp[-(\sigma_{\mathrm{eff}}/\epsilon_{\mathrm{eff}})t] \int_0^t dt' \frac{\exp[+(\sigma_{\mathrm{eff}}/\epsilon_{\mathrm{eff}})t']}{\epsilon_{\mathrm{eff}}} \frac{\partial H_y}{\partial z}, \quad (17)$$

$$E_z = +\exp[-(\sigma_{\mathrm{eff}}/\epsilon_{\mathrm{eff}})t] \int_0^t dt' \frac{\exp[+(\sigma_{\mathrm{eff}}/\epsilon_{\mathrm{eff}})t']}{\epsilon_{\mathrm{eff}}} \frac{\partial H_y}{\partial x}. \quad (18)$$

Thus a pulse experiences nonlinear dissipation unless $\sigma_{\mathrm{eff}} < 0$. Nonlinear growth occurs in that negative resistivity region; it occurs only where χ^{NL} is decreasing in time, i.e., when $\partial_t \chi^{\mathrm{NL}} < 0$. From Eq. (12), this occurs where $\chi^{\mathrm{NL}}/[\epsilon_2 |\mathbf{E}|^2] > 1$. The boundary between the growth and the decay regions occurs where $\sigma_{\mathrm{eff}} \propto \partial_t \chi^{\mathrm{NL}} = 0$, i.e., where $\chi^{\mathrm{NL}} = \epsilon_2 |\mathbf{E}|^2$. Since the longitudinal spatial derivative ∂_z and the scaled time derivative $-\partial_{ct}$ yield similar results for a traveling wave, Eq. (1) or (17) then indicates that the behavior of E_x should be nearly coincident with that of H_y except where the axial component E_z is large. Assuming excitation with a symmetric space–time pulse, there should be a negligible value of E_z along the propagation axis. The maximum E_z should occur off axis where the transverse variation in H_y is a maximum. Thus, at the negative-resistivity region boundary along the propagation axis, this means that $\partial_t \chi^{\mathrm{NL}} \sim E_x \partial_t E_x \sim 0$ and hence that $E_x \approx Z_0 H_y \sim 0$ there. The resulting minima in both transverse components should coincide only in the instantaneous limit where the relaxation time $\tau \to 0$. The possibility of reflections from the focusing region is now revealed, since the longitudinal power flow $S_z = E_x H_y$ can have a null in the focusing region and can subsequently change sign, particularly when $\tau \to 0$. From Eq. (3) we see that the maximum of E_z will occur off axis in this region where H_y, and hence $\partial_x H_y$, experiences its minimum along the z direction, i.e., where $\partial_t E_z \sim 0$. The transverse power flow $S_x = -E_z H_y$, necessary for focusing to occur, should reach its maximum value there as well. The intensity is channeled into the region behind the negative-resistivity boundary, causing an increase in the index of refraction and a corresponding decrease in the wave speed. An increasing separation between the linear and the nonlinear portions of the pulse then occurs. The focusing of the off-axis transverse components will cause the lagging peak to increase until the maximum intensity and the minimum waist occur. The transverse power flow then changes direction as the transverse field component H_y changes sign as it passes through the focal region, and the lagging pulse then begins to expand. The focusing process will start again as the longitudinal field component has a corresponding sign change and begins to grow nonlinearly large, forcing the intensity to flow back toward the propagation axis. However, since energy is being carried away by the leading edges of these focal regions at speeds slightly faster than the focal regions themselves, there is less energy present for each successive focusing region. This causes the resulting peak intensities values to decrease. The frequency of occurrence of these focal regions depends directly on the response time of the medium and the peak intensity of the input pulse.

From the TM first-order set of equations, one can readily derive the following second-order equation for the electric field:

$$\partial_z^2 \mathbf{E} - \mu_0 \epsilon_{\mathrm{eff}} \partial_t^2 \mathbf{E} + \partial_x^2 \mathbf{E} - 2\mu_0 \sigma_{\mathrm{eff}} \partial_t \mathbf{E} - (\partial_{ct}^2 \chi^{\mathrm{NL}}) \mathbf{E} = -(1/\epsilon_0) \nabla (\nabla \cdot \mathbf{P}^{\mathrm{NL}}). \quad (19)$$

Similarly, since $\nabla \cdot \mathbf{E} = -\nabla \cdot \mathbf{P}^{\mathrm{NL}}/\epsilon_0 \equiv 0$ in the TE case, the TE first-order set of equations simply yields the relation

$$\partial_z^2 \mathbf{E} - \mu_0 \epsilon_{\mathrm{eff}} \partial_t^2 \mathbf{E} + \partial_x^2 \mathbf{E} - 2\mu_0 \sigma_{\mathrm{eff}} \partial_t \mathbf{E} - (\partial_{ct}^2 \chi^{\mathrm{NL}}) \mathbf{E} = 0. \quad (20)$$

From Eqs. (19) and (20) one can identify several wave processes. The first two terms represent the longitudinal wave operator, with the speed of the wave packet $v^{-2} = n^2/c^2 = \mu_0 \epsilon_{\mathrm{eff}}$ being controlled by the nonlinearity. This field dependence of the speed produces the nonlinear self-focusing effects. The third term provides for the transverse linear diffraction of the field; the fourth represents a nonlinear loss term. The fifth term produces the nonlinear dispersive effects of the medium. The source term of the final expression shows that the transverse E_x

and longitudinal E_z electric-field components are coupled and driven by the nonlinear polarization effects of the medium.

These second-order expressions suggest the relationship of the full-wave approach to the scalar models. In particular, the scalar models ignore the source term in the TM equation, Eq. (19), and hence the resultant coupling between the transverse and the longitudinal field components. Moreover, for temporal solitons the scalar models reduce the second-order z derivative of the field to a first-order term by means of the standard envelope assumption. One may then interpret the second-order time derivative as a dispersive correction term. On the other hand, an envelope assumption would reduce the TE equation, Eq. (20), to the standard form used to obtain spatial solitons. The present analysis incorporates the commonly ignored terms and makes no envelope assumption in either case. Thus we anticipate that the full-wave, vector Maxwell equation approach in both the TM and TE cases will fully encompass the effects generally contained in the scalar models as well as several others arising from the higher-order derivative terms and the vector properties.

NUMERICAL SOLUTION OF THE NONLINEAR MAXWELL'S EQUATIONS

To obtain a FDTD solution of, for instance, the TM system of Eqs. (1)–(8) and (13), we discretized space into square cells wih dimensions Δx and Δz. The electric-field components are taken along the edges of each cell, which are located at points $(i\Delta x, j\Delta z)$; the magnetic-field components are located at the center of each cell, $[(i + 1/2)\Delta x, (j + 1/2)\Delta z]$. Time is also discretized with increments Δt. The equation set is directly integrated forward in time with a leap-frog technique.[22] The electric-field components are updated at integer increments of the time step, $n\Delta t$, and magnetic-field components at half-integer increments of the time step, $(n + 1/2)\Delta t$. The effective susceptibility χ^{NL}, the effective permittivity ϵ_{eff}, and the effective conductivity σ_{eff} are taken to be at the same location and time as the magnetic-field components. The nonlinear electric-field terms at the cell centers at the half-integer time steps are obtained by forming the average of each electric field component from its two values at the edges of the cell at the previous integer time step, e.g.,

$$E_x(\mathbf{r}_{center}, t_{center}) \rightarrow (1/2)\{E_x[(i + 1/2)\Delta x, j\Delta z, n\Delta t] + E_x[(i + 1/2)\Delta x, (j + 1)\Delta z, n\Delta t]\}, \tag{21}$$

and squaring those averages values, e.g., to give $|E_x|^2$ and summing them to form the complete term $|\mathbf{E}|^2 = |E_x|^2 + |E_z|^2$. The mixed medium-field terms are treated by taking the material properties at the edges of a cell to be the same as those associated with the cell center and by averaging over the electric fields at the two surrounding time points, e.g.,

$$(\epsilon_{eff}/\sigma_{eff})(\mathbf{r}_{center}, t_{center})E_x(\mathbf{r}_{center}, t_{center}) \rightarrow (1/2)(\epsilon_{eff}/\sigma_{eff})[(i + 1/2)\Delta x, (j + 1/2)\Delta z, (n + 1/2)\Delta t] \times \{E_x[(i + 1/2)\Delta x, j\Delta z, n\Delta t] + E_x[(i + 1/2)\Delta x, j\Delta z, (n + 1)\Delta t]\}. \tag{22}$$

Combining these constructs, one obtains from Eq. (2), for instance,

$$E_x[(i + 1/2)\Delta x, j\Delta z, (n + 1)\Delta t] = \frac{1}{A(i,j,n)}\left(-\left\{\frac{H_y[(i + 1/2)\Delta x, (j + 1/2)\Delta z, (n + 1/2)\Delta t]}{\Delta z} - \frac{H_y[(i + 1/2)\Delta x, (j - 1/2)\Delta z, (n + 1/2)\Delta t]}{\Delta z}\right\} + B(i,j,n)E_x[(i + 1/2)\Delta x, j\Delta z, n\Delta t]\right), \tag{23}$$

where the coefficients are

$$\frac{1}{2}[A(i,j,n) + B(i,j,n)] = \frac{\epsilon_{eff}[(i + 1/2)\Delta x, (j + 1/2)\Delta z, (n + 1/2)\Delta t]}{\Delta t}, \tag{24a}$$

$$\frac{1}{2}[A(i,j,n) - B(i,j,n)] = \frac{\sigma_{eff}[(i + 1/2)\Delta x, (j + 1/2)\Delta z, (n + 1/2)\Delta t]}{2}. \tag{24b}$$

The remaining FDTD equations follow in a straightforward fashion.

The TM problem is initiated by driving the tangential magnetic-field H_y field components at $z = +\Delta z/2$ in front of a perfect electric conductor at the simulation region boundary $z = 0$. These source (incident field) terms generate a wave that propagates into the numerical simulation space $z > 0$. The total field is calculated within this simulation region as a sum of this incident field and any scattered fields. This approach minimizes the numerical artifacts that arise from the finite-aperture (nonplane wave) incident field. In the TE case the tangential electric field E_y is driven in front of a perfect magnetic wall.

We have found this FDTD scheme to be numerically stable. It is known to be second-order accurate in the linear domain; the accuracy order in the nonlinear case is unknown at this time.

NUMERICAL RESULTS

The numerical problem deals with two space dimensions and time. The direction of propagation is along z; the transverse direction is along x. The computational grid is excited by driving the initial transverse boundary with a Gaussian weighted (in space), raised cosine (in time) pulse:

$$H_y(x, z = 0, t) = H_0 \exp[-(x/w_0)^2]G(t), \tag{25}$$

where

$$G(t) = \begin{cases} 1.0 - \cos(\omega_0 t) & \text{for } 0 \le t \le T \\ 0 & \text{for } t > T \end{cases}, \tag{26}$$

where $\omega_0 = 2\pi/T$. If the medium were simply a nonlossy dielectric, the numerical Maxwell's equations solver would then generate and numerically simulate the propagation of a pulsed Gaussian beam whose initial waist is defined by the Gaussian weighting function. The initial waist

was taken to be $w_0 = 10.0$ μm. The Fourier transform of $G(t)$ is

$$\tilde{G}(\omega) = \exp(i\omega T/2)\,\frac{\sin[(\omega/\omega_0)\pi]}{\omega}\,\frac{1}{1-(\omega/\omega_0)^2}. \tag{27}$$

The pulse length was taken to be $T = 20.0$ fs. Thus the 6-dB amplitude rolloff point of this spectrum is located at $\omega = \omega_0$, or $f_0 = 1/T = 5.0 \times 10^{13}$ Hz ($\lambda_0 = c/f_0 = 6.0$ μm). The $1/e$ rolloff point is at $f \approx 1.18\, f_0 = 5.9 \times 10^{13}$ Hz. The first null in this spectrum occurs at $\omega = 2\omega_0$, or $f = 1.0 \times 10^{14}$ Hz. The initial pulse actually contains wavelengths of relevance that range in free space from more than 10.0 μm to less than 1.0 μm. We note that the choice of the initial pulse is arbitrary; any continuous, finite-time pulse can be used with the FDTD approach as long as the spatial and temporal resolution is high enough to capture the relevant physics. The raised cosine pulse was chosen for its simplicity.

Because our input pulse is quite narrow and hence has a broad frequency bandwidth, the estimate of the location of the nonlinear focus and the associated focused beam waist cannot be obtained with the standard formulas, since a unique choice of wavelength or frequency cannot be made. Moreover, the nonlinear medium will drastically change the propagation speeds of these various frequency components and hence the actual wavelengths in the medium. In addition, recent results[23] for the propagation of ultrawide-bandwidth pulsed Gaussian beams have shown that the intensity and the energy profiles of the beam are not the same. Thus some care must be exercised in determining the critical focal distance and the initial electric-field strength.

For the simulation runs we set the nonlinear medium parameter to the value $n_2 = \epsilon_2/(2n_0) = 1.0 \times 10^{-18}$ (m^2/V^2), where $n_0 = 1.0$, and we set the input electric-field amplitude to $E_0 = 18.25 \times 10^8$ (V/m). We note that the index of refraction choices do not correspond to a particular material, but they are chosen simply as a representative case. It would be a straightforward matter to tailor the problem to specific materials. The calculation is limited simply by the amount of available computer memory. Suited to the resources available to us, these values simplified the analysis of the results and ensured that the focusing would occur near the center of the computational grid.

The effective frequency of the excitation pulse, which was shown[23] to be a good measure of the frequencies involved in the diffraction process for a broad-bandwidth pulse, is $f_{\rm rad} = f_0/\sqrt{3} = 2.89 \times 10^{13}$ Hz; the corresponding free-space wavelength $\lambda_{\rm rad} = 10.39$ μm. The associated Rayleigh distance for an aperture-driven, raised cosine, pulsed beam is then

$$L_R = \frac{\pi w_0^{\,2}}{\lambda_{\rm rad}} = 30.24\ \mu{\rm m}, \tag{28}$$

which has been confirmed by numerical simulation.[23] If a narrow-bandwidth signal with amplitude E_0, initial waist w_0, and center frequency $f_{\rm rad}$ propagates in a nonlinear medium, its self-focusing distance is then $\sim(E_{\rm cr}/E_0)L_{\rm R}$, where in the instantaneous-response regime

$$E_{\rm cr} = (n_2/n_0)^{-1/2}\lambda_{\rm rad}/(\pi w_0) = 3.307 \times 10^8\ ({\rm V/m}) \tag{29}$$

is the critical field amplitude. Thus, with the indicated parameters, the self-focusing distance would be 5.48 μm. This result has been found to be a large underestimate of the critical nonlinear self-focusing distance. We find that the following reasoning provides a better estimate in the pulse case.

Self-focusing occurs because of changes in the index of refraction of the medium and hence in the speed of propagation and wave numbers in that medium. The distance over which the focusing process occurs changes as the field strengths are varied, but the time for focusing to occur does not. Thus the focusing should occur at the time

$$\mathcal{T}_R = \frac{L_R}{c} = \frac{\pi w_0^{\,2}}{c\lambda_{\rm rad}} = 100.8\ {\rm fs}. \tag{30}$$

Moreover, the intensity pattern of the raised cosine beam expands not at the cw rate, $\theta_{\rm int}^{\rm cw} = \lambda_{\rm rad}/(\pi w_0)$, but rather at the rate

$$\theta_{\rm int} = 8.317^\circ \approx 0.439\,\frac{\lambda_{\rm rad}}{\pi w_0}, \tag{31}$$

the specific value having been obtained here numerically as in Ref. 23. The critical focal distance is then more appropriately defined by

$$z_{\rm cr} \approx \frac{w_0}{\theta_{\rm int}} = 68.89\ \mu{\rm m}, \tag{32}$$

which takes into account the actual beam spread rate. Therefore we would expect the critical focus in the instantaneous response cases to occur at

$$z_f = \left(\frac{E_0^{\rm cr}}{E_0}\right) z_{\rm cr} = 12.48\ \mu{\rm m}. \tag{33}$$

Since a portion of the pulse would not experience the nonlinearity in a finite-response-time case, we would expect the critical focus distance to be bound by the value z_f and the value $c\mathcal{T}_R = L_R$.

Because of the complicated processes that occur in the focal region when multiple frequencies are already present in the pulse, the nominal 1.0λ rule of thumb[10] for the focused waist is no longer applicable. Since the full-wave vector treatment allows for reflections from the focal region and other conversion processes, the final frequency spectrum available for determining an effective frequency parameter is also not available *a priori*. We simply anticipate that, when the medium is responding nearly instantaneously, the waist of the focused beam should be of the order of $\theta_{\rm int} \times c\mathcal{T}_R = 4.39$ μm or less.

Transverse Magnetic

Several TM cases were considered with the medium response time τ with respect to the input pulse width T. In particular, we ran cases with $T = 0.2\tau$, $T = 2.0\tau$, $T = 5.0\tau$, and $T = 20.0\tau$, i.e., $\tau = 100.0$ fs, $\tau = 10.0$ fs, $\tau = 4.0$ fs, and $\tau = 1.0$ fs, respectively. These choices provided access to the nonlinear phenomena associated with mediums exhibiting either finite or instantaneous response times.

Several grid sizes have been used to explore the numerical stability and accuracy of the approach. Direct com-

parisons were made between simulations with a 600 × 800 grid, where $\Delta x = \Delta z = 0.05$ μm or 30.0 μm × 40.0 μm, and a 1500 × 2000 grid, where $\Delta x = \Delta z =$ 0.020 μm or 30.0 μm × 40.0 μm. These discretizations provided a spatial resolution of $\Delta z = \lambda_0/120$ and $\Delta z = \lambda_0/300$, respectively. The coarser resolution was adequate to minimize the numerical dispersion effects in the cases treated; the finer grid simply reduced them further. A Courant stability condition (the time step must be chosen for a two-dimensional problem with $\Delta x = \Delta z$ so that $\Delta t \leq \Delta z/\sqrt{2}c$) or $\Delta z/c\Delta t = 0.38$ was maintained in both cases, which means that we chose $\Delta t = 0.045$ fs and $\Delta t = 0.018$ fs, respectively. The enhanced spatial resolution provided a better resolution of the sharp field patterns that are formed in the focal regions; that is, it reduced the numerical noise. The algorithm did not model the physics well when it was run at the linear equation Courant limit, but it did well for values $\Delta z/c\Delta t \leq 0.50$. The nonlinear version of the Courant limit is not known at this time. With four unknowns and additional overhead, the corresponding total memory requirement was approximately 3.0 Mwords and 10.0 Mwords, respectively. The time requirement is proportional to the number of unknowns and the number of time steps. The 10.0-Mword problem took approximately 510 min of Convex C240 CPU time to compute 7550 time steps, approximately 0.5 μs per unknown. In terms of the problem parameters, this rate corresponds to the pulse's propagating 40 μm ~ $7cT$ with a resolution of 240 cells over the spatial pulse width $cT = 6.0$ μm. The run time would be approximately a factor of 10 less for a single processor of a Cray YMP/8-32 computer.

We found that the self-focusing distance Z_{sf}, i.e., the axial distance to the point at which the maximum intensity occurred, was between z_f and L_R, as expected. However, in each case the time at which the focusing occurred for the cases considered was $\sim\mathcal{T}_R \approx 100.0$ fs. The actual self-focus distance was highly dependent on the ratio T/τ. For $T = 0.2\tau$, the distance $Z_{sf} \sim 24.0$ μm; for $T = 2.0\tau$, $Z_{sf} \sim$ 19.8 μm; for $T = 5.0\tau$, $Z_{sf} \sim 17.1$ μm; and for $T = 20.0\tau$, $Z_{sf} \sim 14.2$ μm. As noted above, the focus locations are drastically different in each of the cases because the wave speeds in their nonlinear regimes are extremely different. Their distances are accurate only to within ±0.45 μm, corresponding to the chosen output frame time spacing of 1.5 fs.

We note that, as anticipated from the full-wave vector analysis, we found that the self-focusing is restrained by the generation of the longitudinal field component and the associated transverse power flow and by reflections from the waveguiding region. The augmented Helmholtz scalar models also predict that the beam will not experience any catastrophic focusing, i.e., will not focus to a point. However, in contrast to the FDTD approach, here the scalar models depend on nonphysical loss mechanisms that limit the self-focusing. In particular, they artificially remove the higher-wave-number components and do not model the important energy-transfer mechanisms between the transverse and the longitudinal field components that occur during self-focusing. The FDTD approach incorporates all beam angles and models the physical flow of power in all directions.

The $T = 0.2\tau$ case is a representative noninstantaneous problem. It illustrates the behavior that subfemtosecond pulsed laser beams, when they become available, will exhibit when they interact with the electronic properties of a material. Because the pulse width is shorter than the relaxation time of the medium, the medium does not have adequate time to respond to the presence of the pulse. Consequently, the front part of the pulse propagates in the medium as a linear beam. Because of this one finds nonlinear decay, not growth, on the front edge of the pulse. The buildup of the nonlinearity occurs in the rising portion of the pulse, causing nonlinear tail effects on the back side of the pulse. The pulse then experiences a mild shock formation with a corresponding creation of a set of upshifted (anti-Stokes) frequency components as it passes into the negative-resistivity region. Focusing occurs to a waist of 3.05 μm for the intensity and 5.05 μm for the total field energy. The pulse breaks up into two packets: the front lobe is broader, hence consisting of the lower frequencies; the back lobe is compressed, thus including the higher, nonlinearly generated frequencies. The front-lobe components travel at speeds different from those of the rear-lobe components because they see a linear rather than a nonlinear medium. The distance between the intensity peaks of these lobes at the time of maximum focus is ~4.0 μm; the front-lobe intensity half-width is ~6.0 μm, and that of the back lobe is ~1.1 μm. The intensity peaks have approximately the same value, the trailing peak being ~1.4 times as large as the leading peak. There is a correspondingly large growth in the longitudinal E_z field component where the null between the lobes in the transverse field components E_x and H_y occurs. The longitudinal component has its peak value off axis at $x = 5.2$ μm. There is no noticeable reflection out of the focusing region, since the medium responds so slowly that the nonlinear channel formation occurs gradually. Rather, the back lobe forms and follows the front lobe, which is diffracted linearly.

The remaining TM cases are (to different degrees) instantaneous-response problems. Thus they are more amenable to comparison with most of the scalar-model results and are more accessible to experimental verification. When $T = 2.0\tau$, we found that the medium responded to the pulse in a fashion similar to the medium in the $T = 0.2\tau$ case but more quickly. Focusing occurs to a waist of 1.25 μm for the intensity and 5.0 μm for the energy. Again, the front edge of the pulse acts in linear manner, i.e., it responds to the presence of a linear medium; the buildup of the nonlinearity occurs on the rising portion of the pulse. The pulse then exhibits a strong shock formation as it passes through the negative-resistivity region, with a corresponding creation of a set of upshifted (anti-Stokes) frequency components. The distance between the intensity peaks of the front and the back lobes is now ~1.1 μm; the front-lobe intensity half-width is ~6.2 μm, and that of the back lobe is ~0.8 μm. The back lobe exhibits a slightly higher intensity than the front lobe, approximately 5.9 times as large. The back lobe develops within a shorter distance, since the medium is responding more quickly to the large field enhancements. The lower-frequency components remain with the front lobe; the higher-frequency components are channeled to the rear lobe. We see a strong growth of the longitudinal component at the cost of the transverse

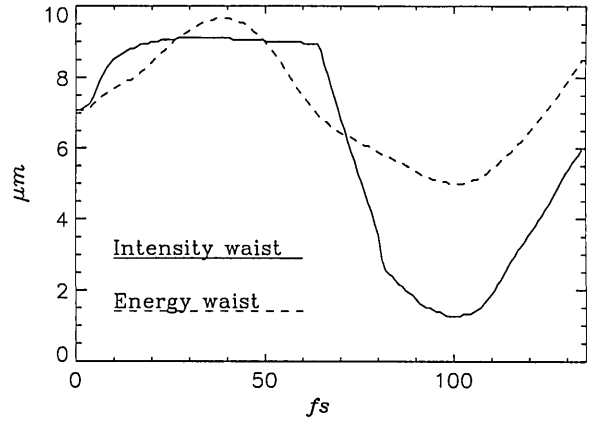

Fig. 1. $1/e$ profiles of the electric-field intensity $I = |E_x|^2 + |E_z|^2$ and the total field energy density integrated along the z axis: $\int dz 1/2\epsilon_{\text{eff}}[|E_x|^2 + |E_z|^2] + 1/2\mu_0|H_y|^2$ versus time are plotted for the $T = 2\tau$ case. The original intensity waist of the input pulse was 7.07 μm.

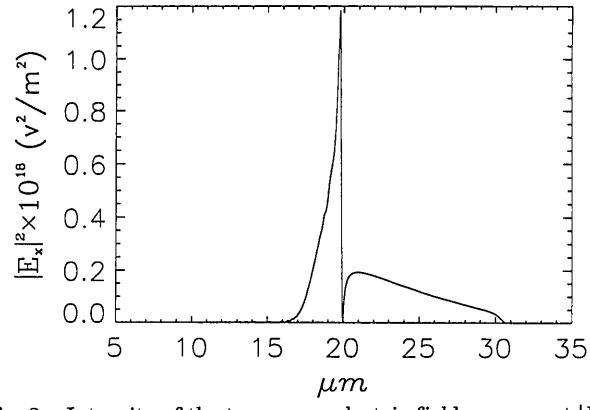

Fig. 2. Intensity of the transverse electric-field component $|E_x|^2$ along the propagation axis, given for the $T = 2\tau$ case at the time $t = 103.0$ fs when the maximum intensity focus occurs.

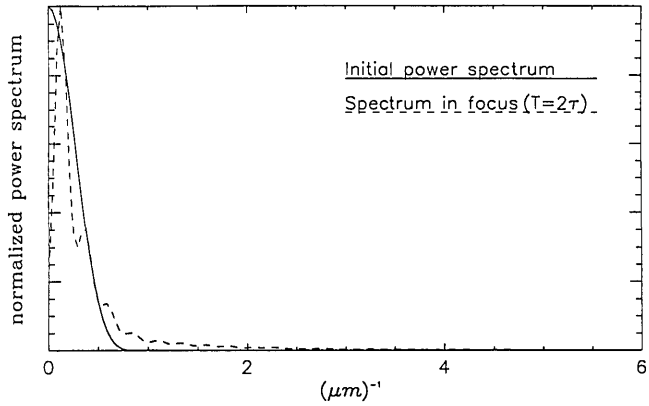

Fig. 3. Power spectrum of the signal $|E_x|^2$ (shown in Fig. 2) along the propagation axis, given for the $T = 2\tau$ case at the time $t = 103.0$ fs when the maximum intensity focus occurs. The power spectrum of the input pulse is given for comparison.

components, and we begin to see some reflection of some longer-frequency components out of the focus region. The longitudinal component has a maximum at $x = 0.72$ μm. The peak value of $|E_x|$, 1.09×10^9 V/m, is 3.30 times the critical value and 3.52 times larger than the peak value of $|E_z|$. There is a corresponding growth in the transverse power flow S_x in the focus region.

Typical results for the $T = 2.0\tau$ case are shown in Figs. 1–8. Plots of the $1/e$ profiles of the electric-field intensity $I = |E_x|^2 + |E_z|^2$ and the total field energy density integrated along the z axis, $\int dx[1/2\epsilon_{\text{eff}}(|E_x|^2 + |E_z|^2) + 1/2\mu_0|H_y|^2]$ versus time, are given in Fig. 1. Note that the initial $1/e$-intensity waist is 7.07 μm, corresponding to the initial amplitude waist $w = 10.0$ μm. As indi-

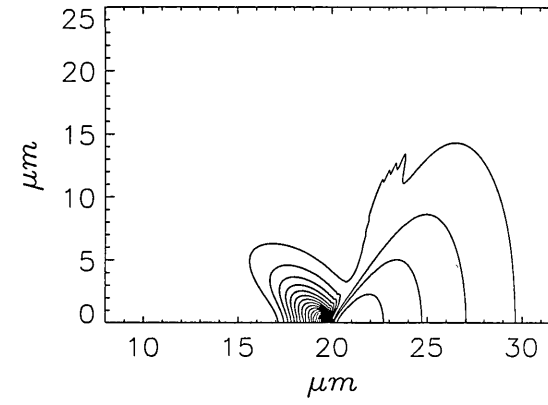

Fig. 4. Contour plot of $|E_x|^2 + |E_z|^2$ for the $T = 2\tau$ case at the time $t = 103.0$ fs when the maximum intensity focus occurs, showing the breakup of the pulse into two lobes, the null appearing in the transition to the negative-resistivity region.

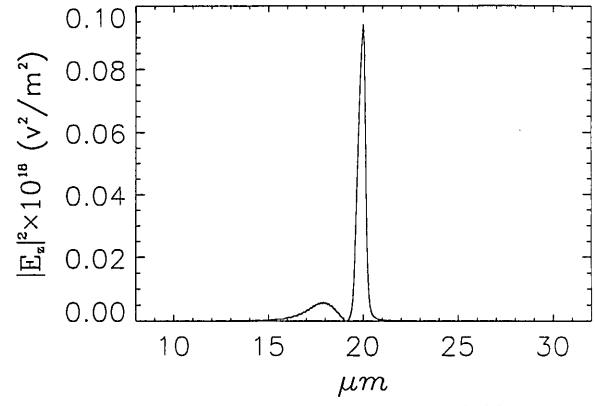

Fig. 5. Intensity of the longitudinal electric-field component $|E_z|^2$ along the axial slice $x = 0.72$ μm, given for the $T = 2\tau$ case at the time $t \sim 103.0$ fs when its maximum value occurs.

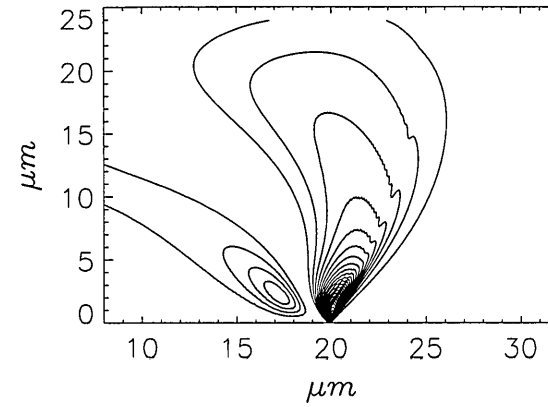

Fig. 6. Contour plot of $|E_z|^2$ for the $T = 2\tau$ case at the time $t \sim 103.0$ fs when its maximum value occurs, showing the appearance of its peak off the propagation axis in the region where the transverse field components exhibit a null.

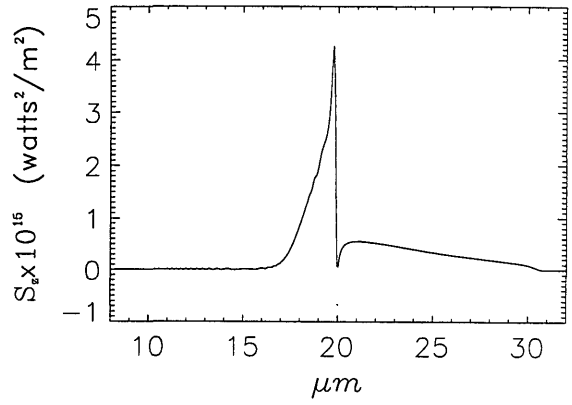

Fig. 7. Longitudinal power flow S_z along the propagation axis, given for the $T = 2\tau$ case at the time $t = 103.0$ fs, corresponding to that when the maximum intensity of the transverse field component E_x occurs.

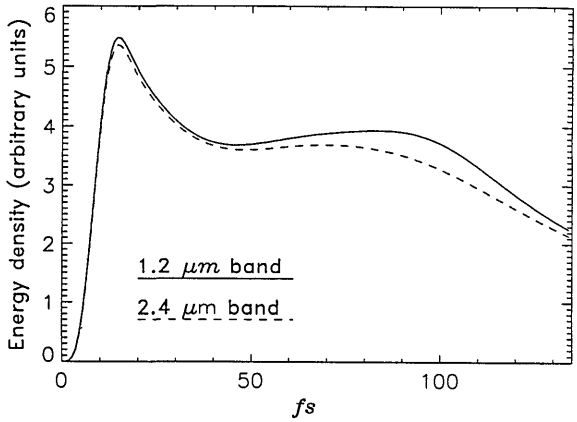

Fig. 8. Total field density $1/2\epsilon_{\text{eff}}[|E_x|^2 + |E_z|^2] + 1/2\mu_0|H_y|^2$ integrated over the spatial band $(x, z) \in [0.0, 1.2\ \mu\text{m}] \times [0.0, 40.0\ \mu\text{m}]$ and over the spatial band $(x, z) \in [0.0, 2.4\ \mu\text{m}] \times [0.0, 40.0\ \mu\text{m}]$ and then normalized to the areas of those bands, plotted versus time for the $T = 2\tau$ case.

cated, the intensity profile is much narrower than the energy profile. This difference results from the spreading of the energy throughout space–time from the focusing process. The intensity is merely a point quantity in any transverse plane; the energy is an average value of the intensity in time. The energy profile is smoother than the intensity curve because it is an average in space of the signal intensity. The initial growth in the profiles occurs because the search for the values occurs over the numerical simulation volume, which does not include the initial boundary values.

Consider Fig. 2, in which the intensity of the transverse electric-field component $|E_x|^2$ along the propagation axis is given at the time $t = 103.0$ fs, corresponding to the maximum intensity focus. Shimizu[4] studied the effect of dispersion on pulse distortion when optical filaments are formed by self-focusing. When normal dispersion is present, the first half of the pulse is compressed, while the tail gradually spreads. An optical shock is eventually formed at the pulse front because of this effect. On the other hand, as anticipated by Shimizu,[4] in nondispersive media the pulse center lags relative to its wings as a result of the nonlinear index. Therefore, as is shown in Fig. 2, the pulse gradually forms a shock at the tail. Similarly, Reintjes *et al.*[5] note that, if dispersion is absent, the leading edge of the pulse does not experience a significant nonlinear index because of the finite response time of the nonlinear medium. Consequently the early part of the pulse diffracts as if the medium were linear. This behavior is characterized by the gradually increasing front lobe (in distance this is the largest z-value portion of the plot) shown in Fig. 2; the intensity increases in the linear area toward the back of the pulse and the nonlinear region. However, because of the integral nature of the transient response, the tendency for focusing increases further into the pulse, causing the diameter to decrease toward the back of the pulse. There is significant distortion of the pulse, resulting in a pulse that is significantly shorter in the high-intensity region than the input pulse duration. The high-intensity region, which is in the rear of the pulse, is formed primarily by the nonlinear index change set up by the early portion of the pulse. Because there is no dispersion, an associated spectral asymmetry occurs, and only upshifted, anti-Stokes frequency components occur from the latter part of the focused pulse. This effect is illustrated in Fig. 3, where the power spectrum of the intensity $|E_x|^2$ shown in Fig. 2 is compared with the power spectrum of the input signal.

A contour plot of the total electric-field intensity $I = |E_x|^2 + |E_z|^2$ in the focal region shown in Fig. 2 is given in Fig. 4. One can see that the high-intensity regions continuously radiate a significant amount of light away at large angles as they propagate. The front (large z) portion corresponds to the linear diffraction region; the rear (smaller z) portion incorporates the nonlinear effects. This horn pattern was first noted by Shen[6,24] for moving-focus effects. Figure 4, however, shows that the actual field structure is more complicated than the simple scalar-equation picture and that two field lobes are formed in the focal region.

The behavior of the longitudinal electric-field component E_z is addressed specifically in Figs. 5 and 6. The maximum intensity of the longitudinal electric-field component $|E_z|^2$ occurs off axis along the axial slice $x = 0.72\ \mu$m and at a time that is slightly larger than the time $t \sim 103.0$ fs when the transverse electric-field component $|E_x|^2$, shown in Fig. 2, achieves its maximum. A plot of $|E_z|^2$ along the axial slice $x = 0.72\ \mu$m when it achieves its maximum is given in Fig. 5. A contour plot of the $|E_z|^2$ intensity field at the same time is shown in Fig. 6. With the corresponding plots of the electric-field intensity given in Figs. 2 and 4, one sees that E_z has grown out of the noise in the transition layer to the negative-resistivity region. Moreover, one can see a second peak appearing in the longitudinal field component. The energy that is transferred out of the focus to the longitudinal field component provides the energy for the next focus. This behavior of the longitudinal field component is unavailable from the scalar models. Its presence is necessary to produce waveguiding conditions in the nonlinear focal region that satisfy Maxwell's equations.

The corresponding axial power density $S_z = E_x H_y$ values along the propagation axis are shown in Fig. 7. A slight negative component occurs in the region of the back lobe. Its shape indicates that it consists essentially of low-frequency, longer-wavelength components that have been reflected back from the waveguiding region. As the leading portion of the pulse transitions through the focal

region there is an associated π phase change in the transverse electric-field component, which provides this sign change. These negative values of the z-directed power of the power flow increase (see Fig. 14 below) as the response becomes more instantaneous; the channel forms faster, causing the reflection coefficients from the channel to increase.

Similar to Feit and Fleck's[10] nonparaxial algorithm for the Helmholtz equation, the FDTD approach is valid for wide-angled beams. In contrast, the FDTD approach accounts for the large-wave-number components, which are lost by the nonparaxial algorithm when self-focusing is developing. No unnecessary evanescent waves are introduced; hence there is no nonphysical loss of power associated with those nonpropagating waves. However, the full-wave vector algorithm does show the anticipated[10] reduced power transmission in the forward direction, which is accompanied by radiation scattered from the nonlinear focal region and the conversion of energy between the transverse and the longitudinal field components. These energy-transfer mechanisms produce the reduced power results from the change in the field patterns as the process of the pulse's focusing, separating, and defocusing repeats itself. The self-focusing process produces the splitting of the field pattern into the linear and nonlinear lobes, causing less energy to be available in any of the lobes in the next focus region. This effective splitting of the pulse is illustrated in Fig. 2. The loss of energy during the focusing process to the nonlinear conductivity term is shown in Fig. 8. The total field energy density $1/2\epsilon_{\text{eff}}[|E_x|^2 + |E_z|^2] + 1/2\mu_0|H_y|^2$, integrated over the spatial band $(x, z) \in [0.0, 1.2\ \mu\text{m}] \times [0.0, 40.0\ \mu\text{m}]$ and over the larger spatial band $(x, z) \in [0.0, 2.4\ \mu\text{m}] \times [0.0, 40.0\ \mu\text{m}]$ and then normalized by the area of those bands, is given versus time. After the initial rise of the average field energy in those bands as the pulse enters the simulation volume, there is a gradual decrease in the field energy as the pulse transitions into the negative-conductivity region. There is an increase of the average energy in the band closer to the axis in the focal region with a corresponding decrease in the larger band. In contrast to the corresponding figures in Ref. 10, there is no abrupt loss of energy after the pulse passes through the focus; rather, there is a steady redistribution of energy back to the larger transverse distances as the pulse unfocuses and a loss of energy to the increased conductivity of the medium.

Figure 9 is a time sequence of plots that illustrates the importance of the growth of the longitudinal field component in the self-focusing process. Contour plots of $|E_x|^2$ and $|E_z|^2$ and the on-axis distributions of the intensity $|E_x|^2$ and the power flux $S_z = E_x H_y$ are given at the times $t = 83.3$ fs, $t = 96.6$ fs, and $t = 109.9$ fs for the $T = 5.0\tau$ case. The first time set occurs long before the first main focus is reached; the second time set is just before the focus time $t \sim 100.0$ fs; and the third time set is an equal interval after the focus. The longitudinal component E_z has already reached a maximum off-axis value in the first time set and, as the pulse propagates, acts as a catalyst for refocusing some of the scattered field energy. The off-axis field energy is also focused as the nonlinear channel grows. As the pulse approaches the true focal region, where its waist reaches a minimum, the peak field pattern exhibits the passage of the pulse through two transition regions. The latter pattern reflects the presence of the intensity focus, the former the initial transition into the negative conductivity region. Following the pulse evolution, the front portion of the pulse corresponds to the original nonlinear transition, the back portion to the focused field intensity. The benign region between both sets simply corresponds to energy carried along with the pulse. The appearance of a second E_z peak is seen in the first time set. The growth of this second peak and the resulting changes in the transverse component are seen from the second set, particularly in the intensity of the transverse field component on axis. Note that the power flux acquires negative values as the focal region is reached. In the third set one can see that a third lobe in the intensity has appeared because of the power that has reflected back out of the focal region. The large off-axis value of E_z is now causing the power to flow away from the focal region, which will eventually feed the next focusing process when it experiences the next channel formation from the front part of the pulse.

When $T = 20.0\tau$ the medium is completely into the instantaneous response regime. The $1/e$ profiles of the electric-field intensity and the total field energy along the z axis are given in Fig. 10. Focusing occurs to a waist of 0.50 μm for the intensity and 1.80 μm for the energy. The field values have become slightly more noisy than in the $T = 2.0\tau$ and $T = 5.0\tau$ cases, since the spatial and temporal resolution has remained the same even though the rate at which changes occur has increased. The energy's profile is smoother than the intensity's, since it is obtained by averaging the intensities over time. The axial slice of the intensity of the transverse electric field $|E_x|^2$ at the focal region time $t = 97.0$ fs is shown in Fig. 11; its power spectrum is compared with the input power spectrum in Fig. 12. The front part of the pulse still diffracts linearly; however, the nonlinearity turns on extremely fast (instantaneous regime), as soon as the pulse amplitude surpasses the critical value early in the computational grid. A corresponding increase in the generation of higher frequencies is observed by comparing Fig. 12 with Fig. 3. A steep shock forms at approximately 6.2 μm, the first transition into the negative-conductivity region. Some reflections of the lower-frequency components are observed from this initial transition region. The resulting pulse exhibits strong tail erosion as the nonlinear conductivity increases quickly in strength. The peak value of $|E_z|$, 1.22×10^9 V/m, is 3.70 times the critical value and 2.40 times larger than the peak value of $|E_z|$. The peak intensity value of the lagging peak is noticeably higher than the forward peak, approximately 2.6 times larger; it is approximately 5.4 times larger than the peak intensity in the linear region. The shape of the back portion of the central region is also quite steep, corresponding to the instantaneous turn off of the nonlinearity. Turn-off occurs when enough energy has left the focal region because of the resulting transverse power flow and additional reflections from the nonlinear channel. There is a corresponding peak of E_z in the region near this rear transition. A plot of the intensity of the longitudinal electric-field component $|E_z|^2$ in the focal region along the axial slice $x = 0.24$ μm for the focal region time $t = 97.0$ fs is given in Fig. 13. The locations of the peaks of this component occur precisely where the derivative behavior in the transverse components is found. Again, the lack of the beam's focusing to a point can be readily connected to

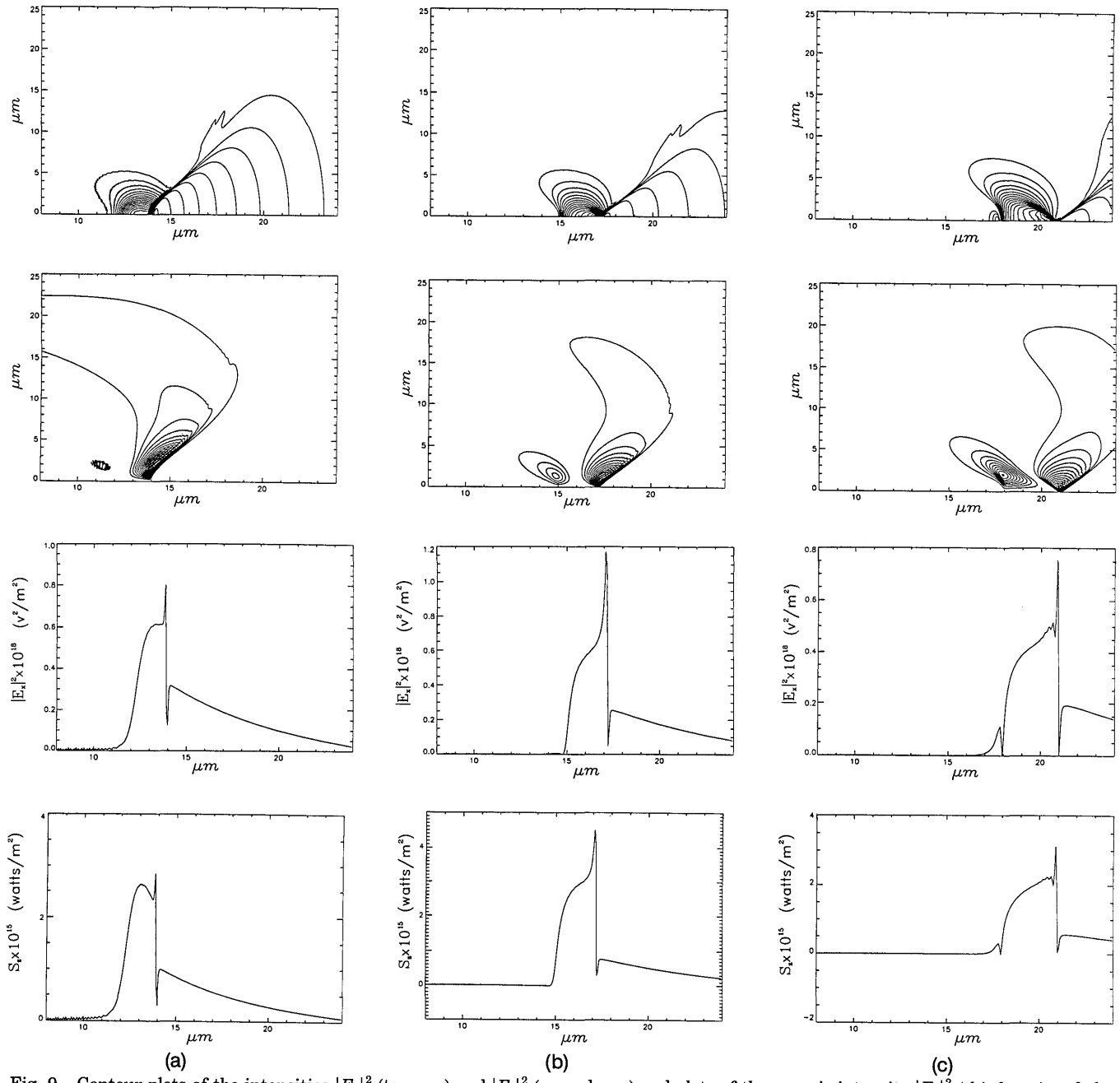

Fig. 9. Contour plots of the intensities $|E_x|^2$ (top row) and $|E_z|^2$ (second row) and plots of the on-axis intensity $|E_x|^2$ (third row) and the power flow density $S_z = E_x H_y$ (bottom row) are given for the $T = 5\tau$ case at times (a) $t = 83.3$ fs, (b) $t = 96.6$ fs, and (c) $t = 109.9$ fs.

the appearances of these peaks; they correspond to energy taken away from the focal region and the axis of propagation. The power flux S_z, when the focal time $t = 97.0$ fs is reached, is shown in Fig. 14. The negative power flux is readily apparent now. As in the $T = 5.0\tau$ case shown in Fig. 9, the appearance of small lagging lobe in Fig. 11 is caused by the negative power flow from the focal region. The total field energy density $1/2\epsilon_{\text{eff}}[|E_x|^2 + |E_z|^2] + 1/2\mu_0|H_y|^2$, integrated over the spatial band $(x, z) \in [0.0, 1.2\ \mu\text{m}] \times [0.0, 40.0\ \mu\text{m}]$ and over the larger spatial band $(x, z) \in [0.0, 2.4\ \mu\text{m}] \times [0.0, 40.0\ \mu\text{m}]$ and then normalized by the areas of those bands, is plotted versus time in Fig. 15. The significantly higher energy density near the axis in the focal region is illustrated with this figure. The loss of field energy to defocusing and to the lossy nonlinear medium occurs after the focal time $\sim\mathcal{T}_R$ is reached. In contrast to those associated with the results given in Ref. 10, the losses in Fig. 15 do not occur in steps. They are more gradual, particularly in the focal regions, because there are physical loss mechanisms present that provide the energy transfer to the medium.

We note that in the $T = 20\tau$ case the multiple self-focusing regions reported in Ref. 10 are observed. However, the physical picture now has a more complex interpretation than simply that the beam alternately contracts and expands between those focal regions. Each transition region causes sign changes in the field components and a power flow toward and away from the propagation axis, which is facilitated by the presence of the longitudinal field component. Each successive intensity peak is lower because of this redistribution of the wave energy from the transverse to the longitudinal field com-

ponents. Moreover, each successive peak travels at a slower speed because of the ever-increasing nonlinear dispersion, which causes the various components to travel at slower speeds. We expect that the process must eventually limit itself as the peak intensity decreases below the nonlinear threshold.

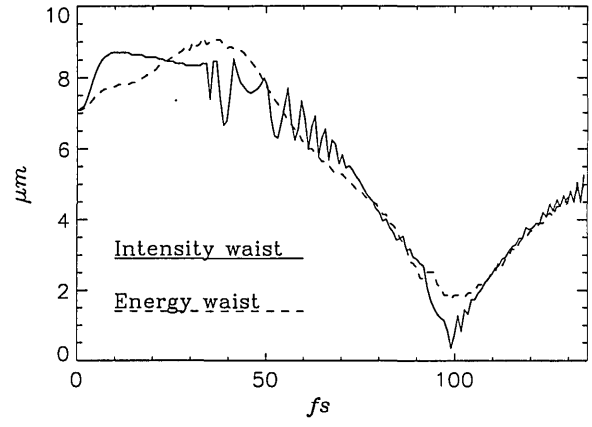

Fig. 10. $1/e$ profiles of the electric-field intensity $I = |E_x|^2 + |E_z|^2$ and the total field energy density integrated along the z axis: $\int dz 1/2\epsilon_{\text{eff}}[|E_x|^2 + |E_z|^2] + 1/2\mu_0|H_y|^2$ versus time, plotted for the $T = 20\tau$ case. The original intensity waist of the input pulse was 7.07 μm.

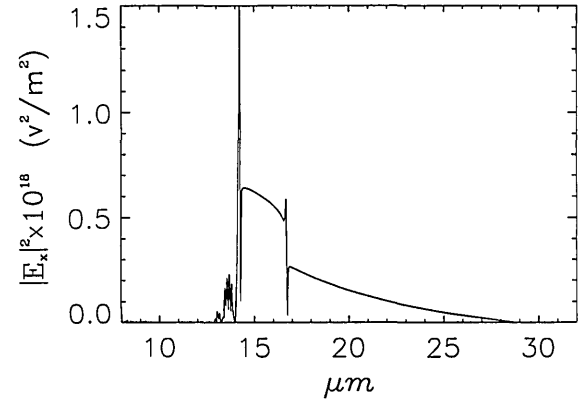

Fig. 11. Intensity of the transverse electric-field component $|E_x|^2$ along the propagation axis, given for the $T = 20\tau$ case at the time $t = 97.0$ fs when the maximum intensity focus occurs.

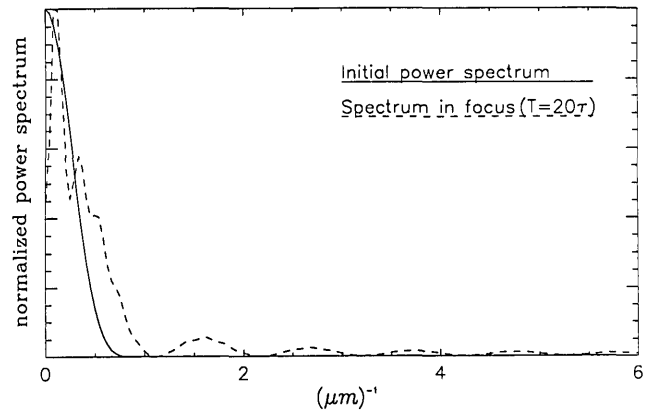

Fig. 12. Power spectrum of the signal $|E_x|^2$ (shown in Fig. 11) along the propagation axis, given for the $T = 20\tau$ case at the time $t = 97.0$ fs when the maximum intensity focus occurs. The power spectrum of the input pulse is given for comparison.

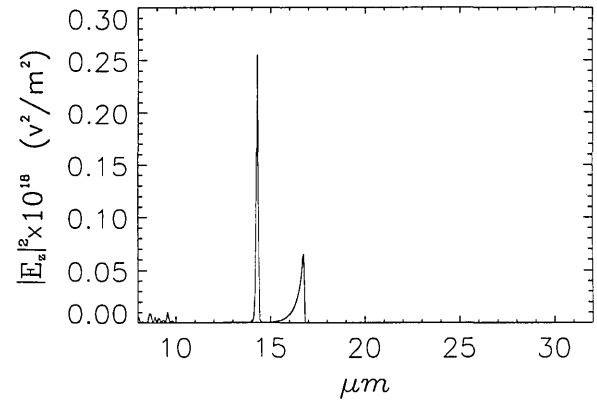

Fig. 13. Intensity of the longitudinal electric-field component $|E_z|^2$ along the axial slice $x = 0.24$ μm, given for the $T = 20\tau$ case at the time $t \sim 97.0$ fs when its maximum value occurs.

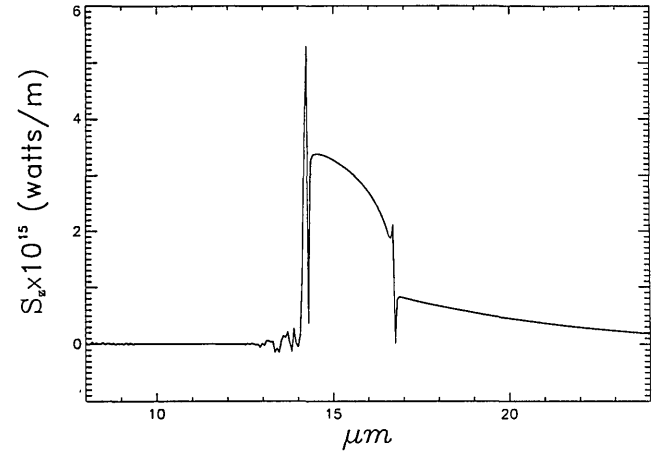

Fig. 14. Longitudinal power flow S_z along the propagation axis, given for the $T = 20\tau$ case at the time $t = 97.0$ fs, corresponding to the maximum intensity of the transverse field component E_x. The negative power flow from energy reflected from the focal region is apparent.

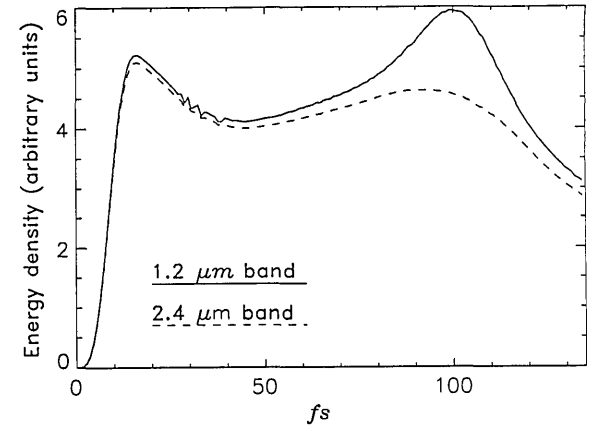

Fig. 15. Total field energy density $1/2\epsilon_{\text{eff}}[|E_x|^2 + |E_z|^2] + 1/2\mu_0|H_y|^2$ integrated over the spatial band $(x, z) \in [0.0, 1.2\ \mu\text{m}] \times [0.0, 40.0\ \mu\text{m}]$ and over the spatial band $(x, z) \in [0.0, 2.4\ \mu\text{m}] \times [0.0, 40.0\ \mu\text{m}]$ and then normalized by the areas of those bands, plotted versus time for the $T = 20\tau$ case.

Transverse Electric

The TE equation set does not exhibit the nonlinear energy transfer phenomena associated with the longitudinal electric field component found in the TM system. Thus we expected and found a quantitatively different behavior for

the TE cases. Consider, for instance, the TE case in which the input pulse width $T = 5.0\tau$, where $\tau = 4.0$ fs. The on-axis values and a contour plot of the intensity $|E_x|^2$ of the transverse electric-field component in the TM case are given in Figs. 16 and 17, respectively, for the focal time $t = 100.0$ fs. The corresponding $|E_y|^2$ plots for the TE case are shown in Figs. 18 and 19, respectively. Although there is no major difference in the peak intensity value, the pulse shapes and their locations and distributions are quite different between the two polarizations. The intensity shown in Fig. 16 exhibits the loss of energy to the longitudinal component on the rear portion of the pulse (z values between ~16 and 17 μm). In contrast, the intensity shown in Fig. 18 is essentially uniform over the length of the original pulse, which surpasses the critical field strength ~3.5 μm. This also explains the difference in the widths of the intensities in the focal regions. Notice that the focus in both the TE and the TM cases occurs at the same time, $t = 100.0$ fs, but not at the same axial distance. The TE case focuses at ~15 μm, whereas the TM case focuses at ~17 μm. Moreover, comparing the contour plots in Figs. 17 and 19, one finds that the field pattern is more diffuse in the TE case than it is in the TM case. This is simply because there are no competing nonlinear mechanisms for the field energy in the TE case. Similar results were found for the other response times.

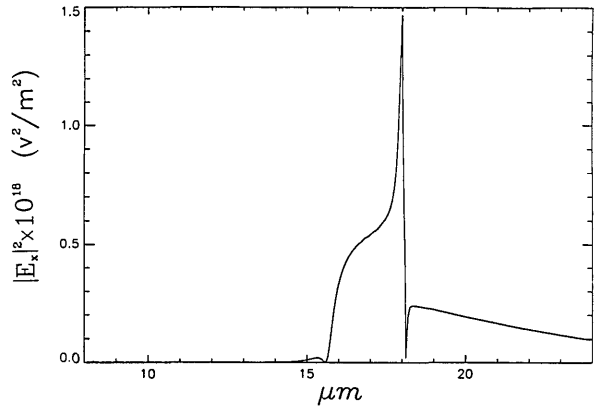

Fig. 16. Intensity of the transverse electric-field component $|E_x|^2$, given for the $T = 5\tau$, TM case at the time $t = 100.0$ fs when the maximum-intensity focus occurs.

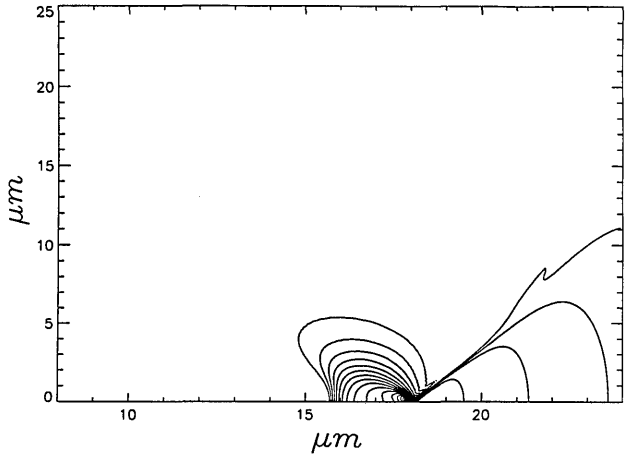

Fig. 17. Contour plot of $|E_z|^2$ for the $T = 5\tau$, TM case, given at the time $t = 100.0$ fs when its maximum value occurs.

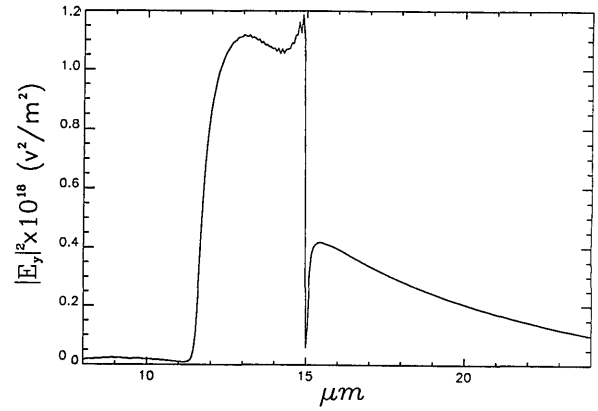

Fig. 18. Intensity of the transverse electric-field component $|E_y|^2$, given for the $T = 5\tau$, TE case at the time $t = 100.0$ fs when the maximum intensity focus occurs.

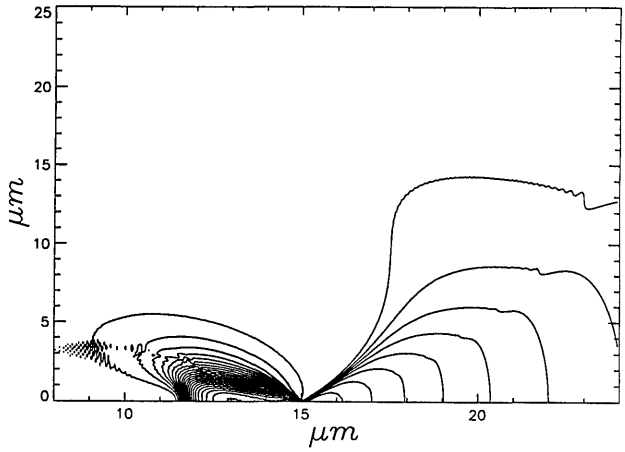

Fig. 19. Contour plot of $|E_y|^2$ for the $T = 5\tau$, TE case, given at the time $t = 100.0$ fs when its maximum value occurs.

CONCLUSIONS AND FUTURE PLANS

We have successfully implemented a nonlinear FDTD algorithm to solve the combined full-wave vector Maxwell and medium-χ^{NL} model equations. The algorithm is stable and cost competitive with conventional scalar approaches. With the resulting numerical simulator we have studied nonlinear self-focusing in a Kerr medium with a finite response time. The full-wave vector treatment recovers many effects predicted by the scalar approaches; however, it has also revealed several unexpected as well as many anticipated results. Of particular interest is the indication that growth of the longitudinal electric-field components occurs and can remove a significant portion of the beam energy from the self-focusing process, thus self-limiting it. With access to more extensive computer resources, we shall be able to examine self-focusing in a fully three-dimensional setting.

In particular, the size of the problem that can be treated with the FDTD approach is machine-memory limited; the more in-core memory, the larger the problem space that one can model. With the parameters used here, a 1000-μm-long problem would require approximately 250 Mwords of memory and 22 single-processor Cray YMP hours to run. However, the FDTD approach maps readily

to a massively parallel environment. Even using only an 8-processor Cray YMP computer, one could optimistically run in less than 3 h such a long-length, nonlinear-optics-waveguide or switch-design problem and include highly detailed information about the local structures in the waveguide or the switch. Simply, the more processors one has, the less time such a problem would take. The fully three-dimensional nonlinear-optics science and engineering design problems of interest will, more than likely, require such a massively parallel computing environment for their successful completion.

Nonetheless, the nonlinear FDTD modeling approach presented here appears to be cost effective for a variety of problems of interest. We shall be able to couple the nonlinear algorithm with existing preprocessing and post-processing capabilities to produce essentially a two-dimensional nonlinear-optics device design code. We shall apply this simulator to modeling the all-optical switching devices, nonlinear waveguides, and nonlinear directional couplers. This research could lead, for instance, to a definitive answer to several outstanding problems, including the engineering potential of a linear–nonlinear interface switch.

ACKNOWLEDGMENTS

The authors express their appreciation and special thanks to Ray Hawkins, Ewan Wright, and Jerry Moloney for their suggestions and insights, which greatly improved our efforts. This research was supported in part by the Lawrence Livermore National Laboratory under the auspices of the U.S. Department of Energy under contract W-7405-ENG-48.

REFERENCES AND NOTES

1. R. Y. Chiao, E. Garmire, and C. H. Townes, "Self-trapping of optical beams," Phys. Rev. Lett. **13,** 479–482 (1964).
2. V. I. Talanov, "Self-focusing of waves in nonlinear media," JETP Lett. **2,** 138–141 (1965) [Zh. Eksp. Teor. Fiz. Pis'ma Red. **2,** 218 (1965)].
3. E. Garmire, R. Y. Chiao, and C. H. Townes, "Dynamics of the self-trapping of intense light beams," Phys. Rev. Lett. **16,** 347–349 (1966).
4. F. Shimizu, "The effect of dispersion on pulse distortion in optical filaments," IEEE J. Quantum Electron. **8,** 851–854 (1972).
5. J. Reintjes, R. L. Carman, and F. Shimizu, "Study of self-focusing and self-phase-modulation in the picosecond-time regime," Phys. Rev. A. **8,** 1486–1503 (1973).
6. For a comprehensive review of experimental work on self-focusing until the mid 1970's, see Y. R. Shen, "Self-focusing: experimental," Prog. Quantum Electron. **4,** 1–34 (1975).
7. J. A. Fleck, Jr., and P. L. Kelley, "Temporal aspects of the self-focusing of optical beams," Appl. Phys. Lett. **15,** 313–315 (1969).
8. For a comprehensive review of theoretical work on self-focusing until the mid 1970's, see J. H. Marburger, "Self-focusing: theory," Prog. Quantum Electron. **4,** 35–110 (1975).
9. S. N. Vlasov, "Structure of the field of wave beams with circular polarization near a nonlinear focus in a cubic medium," Sov. J. Quantum Electron. **17,** 1191–1193 (1987).
10. M. D. Feit and J. A. Fleck, Jr., "Beam nonparaxiality, filament formation, and beam breakup in the self-focusing of optical beams," J. Opt. Soc. Am. B **5,** 633–640 (1988).
11. M. Miyagi and S. Nishida, "TM-type soliton in nonlinear self-focusing media," Proc. IEEE **62,** 1284–1285 (1974).
12. M. Miyagi and S. Nishida, "TM waves in nonlinear self-focusing media," Radio Sci. **10,** 833–838 (1975).
13. D. Pohl, "Vectorial theory of self-trapped light beams," Opt. Commun., **2,** 305–308 (1970).
14. K. Hayata and M. Koshiba, "Full vectorial analysis of nonlinear-optical waveguides," J. Opt. Soc. Am. B **5,** 2494–2501 (1988).
15. D. Pohl, "Self-focusing of TE_{01} and TM_{01} light beams: influence of longitudinal field components," Phys. Rev. A **5,** 1906–1909 (1972).
16. M. S. Sodha, V. P. Nayyar, and V. K. Tripathi, "Asymmetric focusing of a laser beam in TEM_{01} doughnut mode in a nonlinear dielectric," J. Opt. Soc. Am. **64,** 941–943 (1974).
17. K. Hayata, A. Misawa, and M. Koshiba, "Spatial polarization instabilities due to transverse effects in nonlinear guided-wave systems," J. Opt. Soc. Am. B **7,** 1268–1280 (1990).
18. R. Luebbers, F. P. Hunsberger, K. S. Kunz, R. B. Standler, and M. Schneider, "A frequency dependent finite difference time domain formulation for transient propagation in plasmas," IEEE Trans. Electromagn. Compat. **32,** 222 (1990).
19. C. F. Lee, R. T. Shin and J. A. Kong, "Finite difference method for electromagnetic scattering problems," in *PIER4: Progress in Electromagnetics Research*, J. A. Kong, ed. (Elsevier, New York, 1991), Chap. 11.
20. R. M. Joseph, S. C. Hagness, and A. Taflove, "Direct time integration of Maxwell's equations in linear dispersive media with absorption for scattering and propagation of femtosecond electromagnetic pulses," Opt. Lett. **16,** 1412–1414 (1991).
21. P. M. Goorjian and A. Taflove, "FD-TD computational modeling of nonlinear electromagnetic phenomena using a nonlinear convolution approach," presented at the 1991 North American Radio Science Meeting, University of Western Ontario, London, Ontario, Canada; "Direct time integration of Maxwell's equations in nonlinear dispersive media for propagation and scattering of femtosecond electromagnetic solitons," Opt. Lett. **17,** 180–182 (1992).
22. L. Lapidus and G. F. Pinder, *Numerical Solution of Partial Differential Equations in Science and Engineering* (Wiley, New York, 1982), pp. 489–496.
23. R. W. Ziolkowski and J. Judkins, "Propagation characteristics of ultrawide-bandwidth pulsed Gaussian beams," J. Opt. Soc. Am. A **9,** 2021–2030 (1992).
24. Y. R. Shen, *The Principles of Nonlinear Optics* (Wiley, New York, 1984), Sec. 17.4.